Eruptions at Lone Star Geyser, Yellowstone National Park, USA: 1. Energetics and eruption dynamics

Leif Karlstrom,[1] Shaul Hurwitz,[2] Robert Sohn,[3] Jean Vandemeulebrouck,[4] Fred Murphy,[2] Maxwell L. Rudolph,[5] Malcolm J. S. Johnston,[2] Michael Manga,[6] and R. Blaine McCleskey[7]

[1] Geysers provide a natural laboratory to study multiphase eruptive processes. We present results from a 4 day experiment at Lone Star Geyser in Yellowstone National Park, USA. We simultaneously measured water discharge, acoustic emissions, infrared intensity, and visible and infrared video to quantify the energetics and dynamics of eruptions, occurring approximately every 3 h. We define four phases in the eruption cycle (1) a 28 ± 3 min phase with liquid and steam fountaining, with maximum jet velocities of 16–28 m s^{-1}, steam mass fraction of less than ~ 0.01. Intermittently choked flow and flow oscillations with periods increasing from 20 to 40 s are coincident with a decrease in jet velocity and an increase of steam fraction; (2) a 26 ± 8 min posteruption relaxation phase with no discharge from the vent, infrared (IR), and acoustic power oscillations gliding between 30 and 40 s; (3) a 59 ± 13 min recharge period during which the geyser is quiescent and progressively refills, and (4) a 69 ± 14 min preplay period characterized by a series of 5–10 min long pulses of steam, small volumes of liquid water discharge, and 50–70 s flow oscillations. The erupted waters ascend from a 160–170°C reservoir, and the volume discharged during the entire eruptive cycle is 20.8 ± 4.1 m^3. Assuming isentropic expansion, we calculate a heat output from the geyser of 1.4–1.5 MW, which is < 0.1% of the total heat output from Yellowstone Caldera.

1. Introduction

[2] Geysers are intermittently discharging hot springs or fountains driven by steam and/or noncondensable gas. They are rare, with probably less than 1000 worldwide of which approximately half are in Yellowstone's Upper Geyser Basin [*Bryan*, 1995]. This rarity reflects the special conditions needed for their formation: abundant supply of water and heat and a unique geometry of fractures and porous rocks [*White*, 1967; *Ingebritsen and Rojstaczer*, 1993, 1996, *Belousov et al.*, 2013, *Vandemeulebrouck et al.*, 2013]. Some geysers erupt relatively frequently (intervals of minutes to hours between eruptions) and at predictable times, making them a unique natural laboratory to study multiphase eruption processes [e.g., *Kieffer*, 1989; *Thiery and Mercury*, 2009]. An improved understanding of geyser eruption dynamics can yield insight into other self-organized, intermittent processes in nature that result from phase separation and localized input of energy and mass; for example, in volcanoes [e.g., *Woods and Bower*, 1995; *Koyaguchi et al.*, 2010] and on the sea floor [e.g., *Leifer and Macdonald*, 2003; *Sohn et al.*, 2009]. Active geyser-like features have also been observed on Enceladus [e.g., *Porco et al.*, 2006; *Brilliantov et al.*, 2008].

[3] Models for geyser processes have a long history, with contributions as old as *Mackenzie* [1811], *Bunsen* [1847], and *Jaggar* [1898]. Although many studies have focused on subsurface processes that trigger, induce, or initiate the eruption, a few also focus on geyser eruption columns [*Kieffer*, 1984, 1989; *Weir et al.*, 1992]. Eruptions are powered by the rapid conversion of thermal energy contained in the erupting mixture to mechanical energy [*Steinberg*, 1980; *Mastin*,
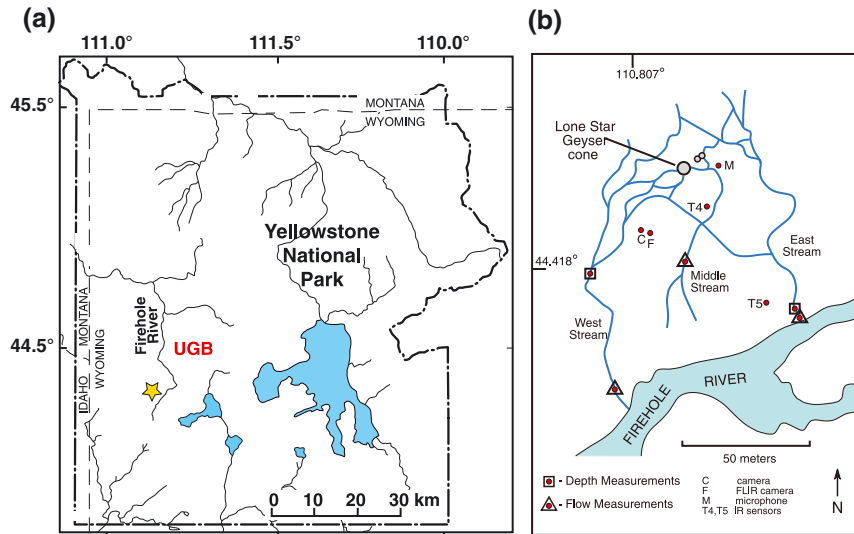

Figure 1. (a) Map of Yellowstone National Park, showing the location of the Upper Geyser Basin (UGB) and Lone Star Geyser (yellow star). (b) Map of Lone Star Geyser experimental setup, showing the location of instruments, the geyser cone and outflow channels.

1995; *Lu and Kieffer*, 2009], with available potential energy depending on temperature, pressure, and noncondensible gas content of the geyser reservoir [*Fournier*, 1969; *Hutchinson et al.*, 1997]. An eruption cycle consists of the build up and release of this potential energy, culminating in rapid fluid discharge through a surface vent. Multiphase dynamics prior to and during eruption result in unsteady jet flow on time scales that range from less than a second to minutes. Unsteady flow consists of oscillations as well as nonperiodic pulsed flow, and is also reflected in near-field seismic signals and harmonic tremor [*Kedar et al.*, 1996] that track boiling processes in the conduit. The dynamic behavior of these systems is important, not just for our basic understanding of geyser processes, but for the efficiency of heat transport from the solid Earth into the atmosphere.

[4] We focus here on poorly characterized aspects of geyser jet dynamics and overall energy budget, using data collected in September 2010 during a 4 day experiment at Lone Star Geyser in Yellowstone National Park (Figure 1). Lone Star Geyser was selected for the experiment because its eruptions are relatively vigorous and voluminous, and because the eruption intervals are relatively short and nearly constant (∼3 h), thereby allowing us to observe 32 eruption cycles over the course of 4 days. In this work, we focus on three questions (1) What are the defining characteristics of the Lone Star eruption cycle? (2) What causes unsteady flow in the erupting jet during the main eruptive phase? (3) How efficiently do geysers transport heat between the hydrothermal system and the atmosphere, and what is their overall contribution to the Yellowstone heat budget [*Hurwitz et al.*, 2012a]? To address the first question, we analyze data from all 32 eruption cycles. To answer the second question, we focus on a particular eruption, addressing the time variation and composition of eruptive products. We also assess vent overpressure and the likelihood of choked flow conditions at the vent. For the third question, we combine water chemistry analysis and thermodynamic calculations to estimate the temperature of the deep reservoir feeding the geyser system.

2. Lone Star Geyser

[5] Lone Star Geyser is located ∼5 km SSE of Old Faithful Geyser at an elevation of 2325 m (Figure 1a). Many small hot springs are located in the immediate vicinity of the cone, and throughout the 4 days of the experiment, we observed qualitatively changes in flow during Lone Star's eruptions. A braided system of shallow streams channels the erupted water to the Firehole River, 75 m to the south of the Geyser (Figure 1b). Lone Star's cone has a diameter of ∼5 m at its base and stands ∼3 m above its sinter terrace (Figure 2a). There are many small apertures in the upper part of the cone ∼1 cm in diameter or less and one main aperture of 20–40 cm in diameter through which the geyser emits most of the liquid water and vapor during eruptions. Conduit geometry is approximated through photographs taken looking down on the vent at an angle of 15–25° from the vertical and containing known objects for scale, and is consistent with descriptions of previous expeditions (Lee Whittlesey, Yellowstone National Park, written communication, 2011). Not all of the apertures are active in all eruptions or through all parts of the eruption cycle.

[6] Although Lone Star is not monitored instrumentally by the Geyser Observation and Study Association like many other geysers in Yellowstone (http://www.geyserstudy.org/), the eruption cycle is regular and has been stable at approximately 3 h since at least 1920 (Lee Whittlesey, Yellowstone National Park, written communication, 2011). However, due to the lack of an instrumental record, it has not been possible to document eruption interval variations in response to seasonal changes [*Hurwitz et al.*, 2008] or earthquakes [*Hutchinson*, 1985; *Husen et al.*, 2004].

3. Experimental Methods

[7] We deployed an array of instruments around the geyser (Figure 1b) to characterize the eruption cycles and erupting column. We briefly summarize instrumentation and methods here, with a more detailed description in
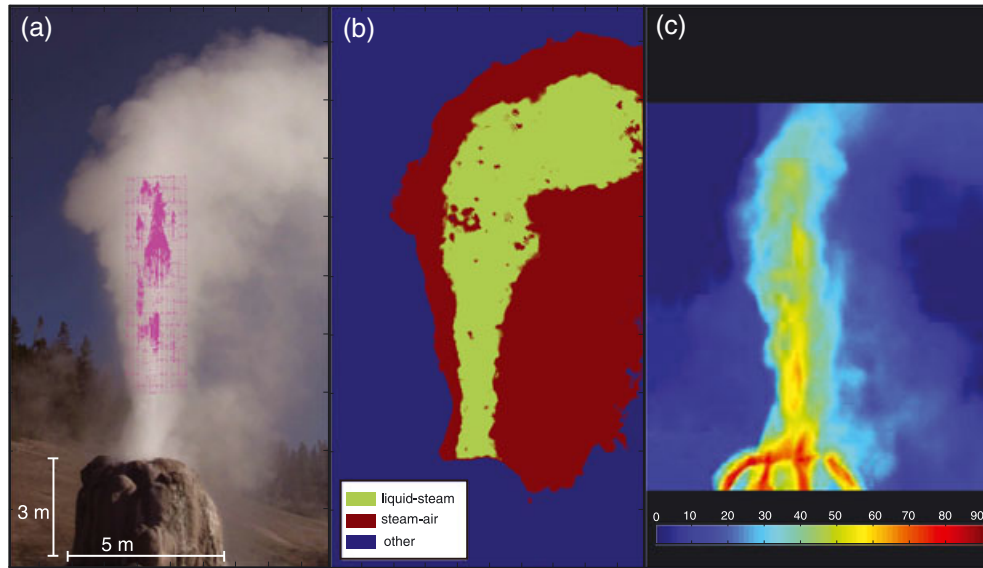
Figure 2. Simultaneous images from ~10 min after the onset of the eruption that began at 15:15:41 UTC 23 September 2010 illustrating (a) visible video with PIV velocity vector overlay. Maximum calculated velocity shown is 18.36 m s^{-1}. (b) Segmented image with liquid and condensed steam dominated fields. (c) Forward Looking Infrared (FLIR) infrared video frame with temperature scale in °C. Note the differences in image size, look angle, and small relative timing difference between FLIR and visible frames.

Appendix B. Eruption times were determined using three Infrared (IR) sensors located around the cone at distances ranging from 5 m to 50 m (Figure 1b) and aimed such that the field of view was just above the geyser outlet. Video was acquired during nine eruptions at visible and infrared wavelengths. We set up a 3 Hz–20 kHz microphone (GRAS company) at a distance of 20 m from the cone, sampled at 1 kHz. We estimated the volume of liquid water discharged from the geyser for each period of the eruption cycle by making stream flow measurements along two of the three main geyser outflow channels for eight eruption cycles.

[8] Water samples were collected during a single eruptive cycle from the two main channels draining the geyser for major element geochemistry. We used the two chemical geothermometers considered the most applicable for the Lone Star water composition to estimate the temperature of the reservoir from which the erupted waters ascended [*Fournier*, 1981]. The quartz adiabatic geothermometer [*Fournier and Rowe*, 1966; *Fournier and Potter*, 1982] is based on the SiO_2 concentration (mg L^{-1}) in the water:

$$T_{\text{Quartz}}(°C) = (1522/(5.75 - \log[SiO_2])) - 273.15 \quad (1)$$

This method explicitly assumes that solubility of quartz is sensitive to temperature and that rates of quartz thermodynamic equilibration are much faster than rates of conductive cooling to the host rock. The second geothermometer is based on the mass ratio of Na$^+$ to K$^+$ [*Fournier*, 1979]:

$$T_{\text{Na–K}}(°C) = (1217/(\log[Na^+/K^+] + 1.483)) - 273.15 \quad (2)$$

[9] Time series of IR and acoustic measurements were used to establish the start and end times of eruptions and to define the eruption cycle (Figure 3). We use these data along with visible and IR video to characterize the spectrum of unsteady flow seen during the main eruptive phase.

Video was processed with particle image velocimetry (PIV) software (using the Matlab based OpenPIV (http://www.openpiv.net)) to determine coarse scale exit velocities, and with image segmentation techniques to calculate jet height and relative ratios of liquid and steam dominated flow. We estimate total erupted volume using PIV velocities and an assumed turbulent jet velocity profile (discussed later). Based on integration window resolution tests (supporting information), we estimate PIV velocity magnitude errors as large as 5–10 m s^{-1} (supporting information, Figure 2) and consider them to be a strict upper bound to velocity magnitude. We find that time variations of the velocity field are more robust than absolute magnitudes (scaling PIV velocity vectors by measured cone height of 3 m and frame rate of 30 Hz).

[10] Visible video offers the opportunity to quantify the variable amounts of steam and liquid that erupt, given the color contrast between condensed steam-air (droplets in air) and liquid-steam (bubbles in liquid) mixtures. Although it is not possible to directly quantify liquid and steam fractions in this manner, we can clearly distinguish color differences between regions with liquid-steam mixtures and more dilute and transparent condensed steam-air mixture regions. We use this method to estimate liquid-dominated jet height and relative liquid to steam ratios through the eruption. To automate the segmentation of these regions through time, we use a common image processing technique on Red Green Blue (RGB) frames (Appendix B). We find the reference values for the "liquid-steam" and "steam-air" regions through machine learning [*Gonzalez et al.*, 2004], then analyze the entire eruption at 3 Hz for number of pixels that fall in each class.

[11] Temperature data derived from Forward Looking InfraRed (FLIR) video (Figure 2c) are processed by choosing a 10 by 10 pixel interrogation window focused on the
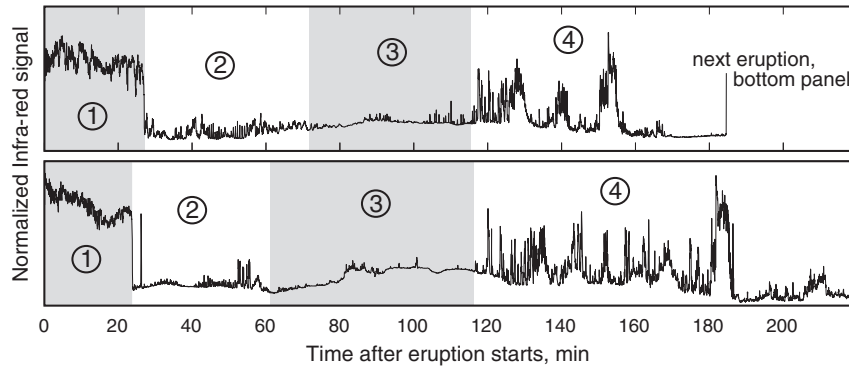
Figure 3. The four-phase eruption cycle illustrated with normalized data from IR sensor 4 for two consecutive eruption intervals. The eruption cycle is divided into four distinct periods: (1) Main eruption, primary discharge of fluid from the vent, (2) Posteruption relaxation, (3) Quiescence in which the system is gradually filling, and (4) Preplay, during which a series of thermal pulses occur along with intermittent surface fluid discharge. Time period shown starts at 04:49:40 UTC on 21 September 2010.

jet above the vent, and picking the maximum and mean temperatures in this window through time. FLIR temperature measurements are limited by condensed steam obscuring the hot core of the jet. Nonetheless, we observe maximum temperatures that are within 6°C of the 93°C boiling temperature at measured atmospheric pressure of 0.75 bar.

4. Results

4.1. The Eruption Cycle

[12] The average Geyser Eruption Interval of 32 consecutive eruptions (using hour: minute notation) was 3:00 h with standard deviation 0:16 h based on the acoustic noise data, and 2:59 ± 0:26 h based on the infrared intensity. These values are similar to historical noninstrumental measurements (Lee Whittlesey, Yellowstone National Park, written communication, 2011), indicating that the timing of the eruption cycles has not changed appreciably for almost 100 years. This eruption interval is also similar, within error, to the period of conductivity variations measured ~100 m downstream of Lone Star geyser in the Firehole river during the study period [*McCleskey et al.*, 2012].

[13] Water discharge measured from outflow channels during nine eruption cycles varied between 15.4 m^3 and 28.1 m^3 with an average of 20.8 ± 4.1 m^3 (supporting information). This discharge includes base stream flow as well as water ejected from the geyser cone. Subtracting the base flow, we find eruptive volumes from the main eruption phase and preplay in the range 9.6 ± 1.0 m^3 and 3.5 ± 1.7 m^3, respectively. Main eruption phase discharge estimates are an upper bound on jet discharge as some water spills on the cone through small side vents and some increased spring discharge occurs during the main eruption phase. More detailed characterization of discharge throughout the eruptive cycle, including timing of increased streamflow, is available in the supporting information.

[14] The major element chemistry, water isotope composition, and calculated reservoir temperatures based on the composition of water samples are presented in the supporting information. Water samples from the eastern channel were collected at the base of the geyser cone, whereas samples from the western channel were collected ~20 m away

from the cone. Water isotopes indicate that samples from the eastern channel represent progressive evaporation during the eruption, so that the first sample collected is the least evaporated and therefore, with the lowest SiO$_2$ concentration (supporting information). All water samples from the western channel have undergone more evaporation compared with water samples from the eastern channel. Using the SiO$_2$ concentration of the first sample from the eastern channel (YNP080412LSE1), the reservoir temperature based on the quartz adiabatic geothermometer is 177°C. However, if we assume that even this first sample has lost 5 or 15 wt% by steam loss during the eruption, then the calculated temperature decreases to 175°C and 168°C, respectively. The average calculated reservoir temperatures based on the Na-K geothermometer derived from 11 samples is 159±5°C, and the reservoir temperature based on sample YNP080412LSE1 is 162°C. Different calculated reservoir temperatures using the two geothermometers are common and result from several processes [*Fournier*, 1981]. For further calculations, we use reservoir temperatures ranging between 160°C and 170°C, which is somewhat lower than the calculated reservoir temperatures in the adjacent Upper Geyser Basin [*Hurwitz et al.*, 2012b].

[15] We divide the Lone Star Geyser eruption cycle into four distinct phases (using IR and acoustic data, Figures 3 and 4) that are evident in all of the eruption cycles observed during our experiment: (1) a 28 ± 3 min long eruptive phase during which liquid and steam discharge through the geyser to form a fountain with maximum height slightly above 12.8 m (the top of our video frame). At the eruption, onset IR intensity is maximum then decreases gradually until the end of the eruption. By contrast, the acoustic power rises more slowly, peaking ~12 min after the eruption start (Figure 4, third panel). For all eruptions in our data set, the peak of acoustic power comes at an average of 10 ± 1 min after eruption onset. (2) A 26 ± 8 min long posteruption relaxation phase that begins immediately after the eruption fountain ceases. During this phase, the IR signal drops off rapidly to background levels, and then oscillates together with the acoustic noise at periods that glide between 30 and 40 s as the system relaxes to ambient conditions (Figure 4). (3) A 59 ± 13 min long recharge period during which the geyser
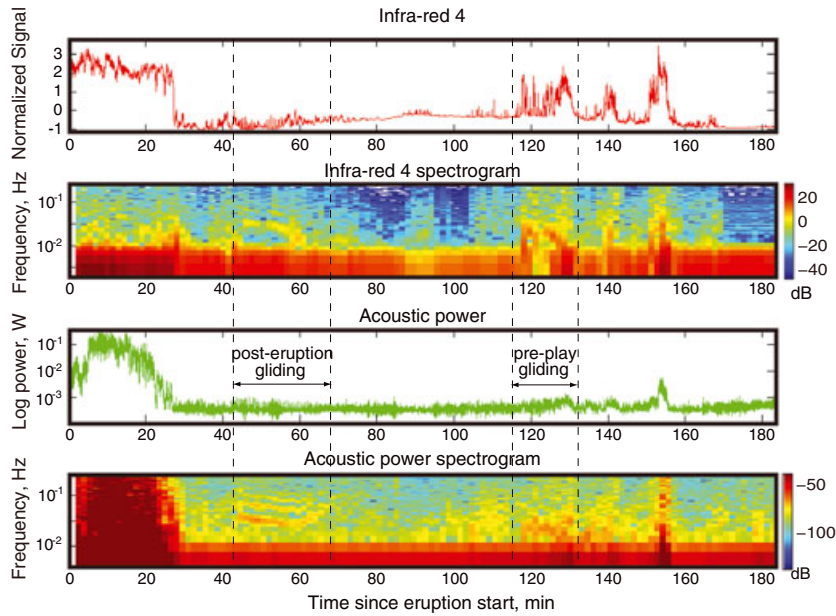
Figure 4. Comparison of IR (infrared sensor 4) and acoustic power for one eruption cycle with corresponding spectrograms, illustrating the gliding periods of oscillation observed in posteruption relaxation and preplay (time windows within dashed lines). Time period shown starts at 07:54:18 UTC on 21 September 2010.

plumbing system progressively refills. (4) A 69 ± 14 min preplay period characterized by a series of 5–10 min long intervals during which puffs of steam and small volumes of liquid water discharge from the vent (evident as increases in IR intensity in Figures 3–5). The number of these pulses varies between one and eight, with an average of three. In between these pulses, we observed synchronized oscillations in the IR and acoustic noise signals at smoothly varying

periods ranging from 50 to 70 s. These distinct phases are similar to those defined by *Kieffer* [1984] for Old Faithful Geyser, although the preplay is longer and more vigorous at Lone Star.

[16] Oscillations in the main phase, posteruption relaxation phase, and preplay phase occur throughout all eruptions, but differ in period and time lag between IR and acoustic signals. During relaxation, the dominant period
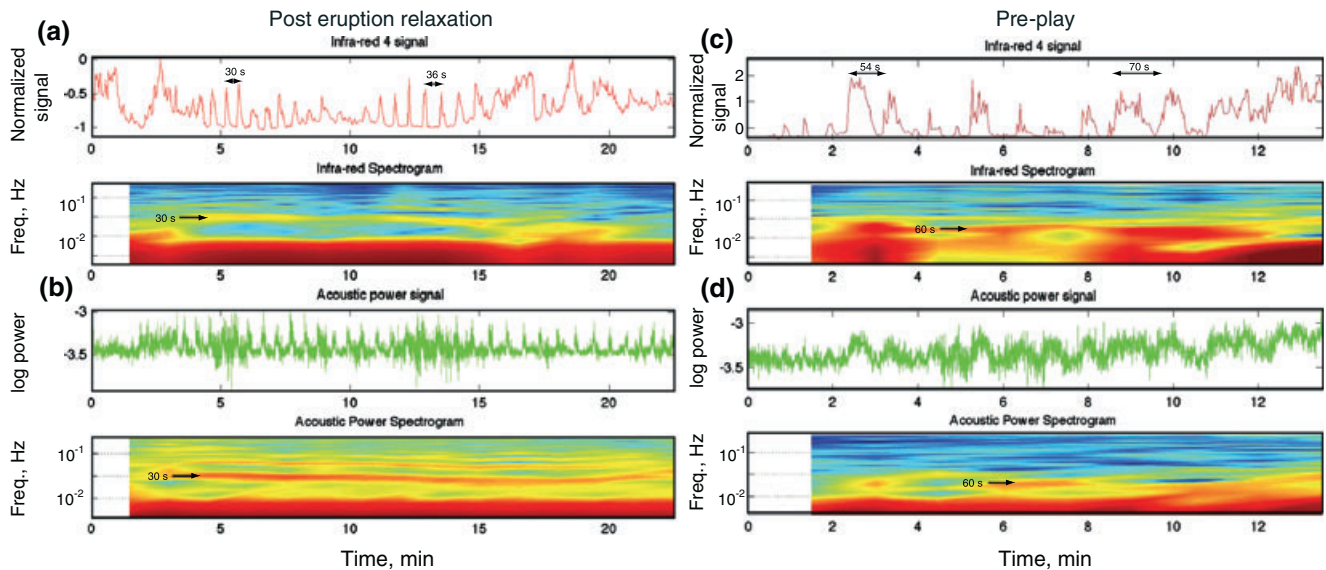
Figure 5. Oscillatory signals in (a and b) posteruption relaxation (start time of 08:36:00 UTC on 21 September 2010) and (c and d) preplay, (start time of 09:50:00 UTC on 21 September 2010) (Figure 4). During posteruption relaxation, oscillations occur with periods in the range of 30–40 s with no corresponding surface discharge. During preplay, longer 50–70 s periods occur with some surface discharge, although discharge is generally not well correlated with oscillatory signals.

Figure 6. Cross correlation between acoustic and IR signals for (a) the preplay period presented in Figure 5 and (b) the posteruption period. The IR signal is simultaneous to the acoustic within the 2 s IR sensor sampling error during preplay, but lags the acoustic signal by 8 s for relaxation (although with weaker correlation coefficient).

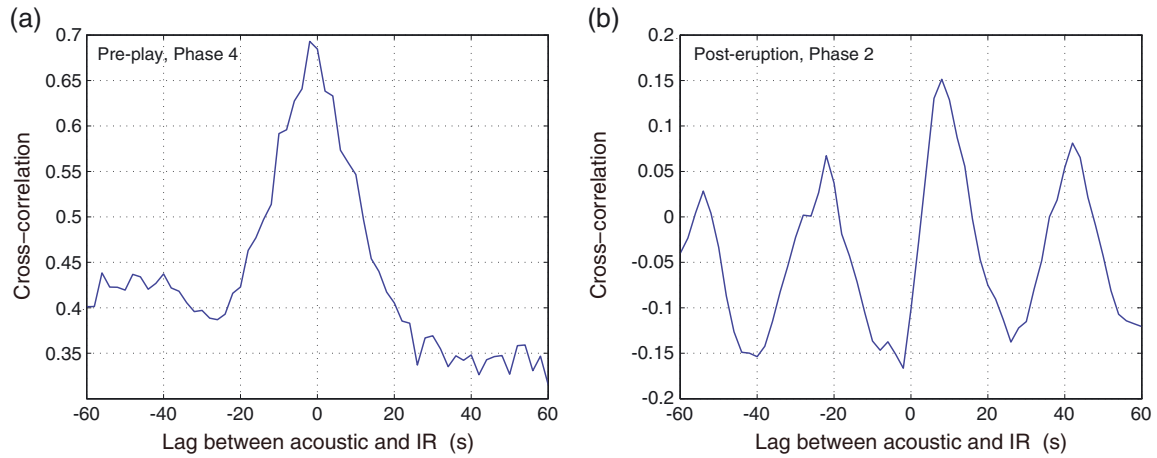transitions between 30 and 40 s (Figure 5a and b). Although the cross-correlation coefficient between IR and acoustic signals is small, there appears to be ~8 s lag between the acoustic and IR signals (acoustic leading IR, Figure 6b). No liquid is discharged from the vent during these oscillations, such that the oscillations appear to represent rising and falling of liquid and steam mixtures in the conduit. The 8 s time lag is consistent with an emptied system for which acoustic signals generated by flow through a subsurface constriction/nozzle lead rising steam pulses. By contrast, the 50–70 s period synchronized oscillations during preplay have no time lag (within sampling error), indicating that the system is relatively full during preplay. As a result, the rise and fall of liquid and steam mixtures in the eruption conduit is synchronous with the subsurface flow noise oscillations. This interpretation is supported by the observation that some surface discharge does occur during the preplay phase, indicating that the conduit fills and overtops with hot fluid during this phase.

4.2. Jet Velocity and Stability

[17] We use data from the best characterized eruption that began on 23 September 2010 at 15:15:41 UTC to study the dynamic behavior of the erupting jet. This is eruption number 23 of our experiment (supporting information). High quality visible video, FLIR, acoustic, seismic time series (Jean Vandemeulebrouck, ISTerre, unpublished data), as well as stream discharge data (8.1 m^3 maximum during phase 1) are all available for this eruption. These simultaneously acquired time series enable us to obtain well constrained estimates for the dominant periods of the eruption cycle processes, and to study the transition from liquid to steam dominated discharge during an eruption as the shallow geyser reservoir empties. Due to instrument malfunction, IR sensor data were not available during this eruption.

[18] The average magnitude of all velocity vectors measured by PIV is generally 5–10 m s^{-1} per frame during the main eruption, while the largest PIV velocities in each frame are at maximum 28 m s^{-1}. There is a considerable high frequency and frame-to-frame noise in velocity magnitude.

This noise can be attributed to projection issues (2-D projection of a turbulent 3-D flow in which the high-velocity core is often obscured) and methodology (we do not require temporal continuity in tracked particles). We expect that more consistent velocity time series could be obtained by combining spatial with temporal cross correlation [*Crone et al.*, 2008]. However, because we are not attempting to understand the detailed turbulent structures of the flow and are concerned with velocity variations for periods of greater than ~1 s, the present method is sufficient. As a check, we compare PIV maximum velocity time series with ballistic velocities derived from jet height (using the height of liquid-steam pixels calculated from image segmentation). This velocity scale, $\sqrt{2gH}$ where g (m/s^2) is gravitational acceleration and H (m) is the height of the liquid dominated jet, neglects drag and buoyancy effects. Still, the two estimates are within a factor of 2 and hence comparable for our purposes (green and purple curves in Figure 7a). We consider ballistic and PIV velocities to generally represent a lower and upper bound, respectively, that are comparable in magnitude to velocity estimates for other large geysers [*Kieffer*, 1989; *Rudolph et al.*, 2012]. However, the fact that ballistic velocities exceed PIV velocities after ~15 min of eruption where steam dominates indicate that the ballistic calculation likely over-estimates exit velocity when buoyancy rather than inertia drives the flow.

[19] Concurrent measurements of jet maximum velocity, temperature, jet height, image analysis of liquid content, and acoustic power show remarkable consistency throughout the main phase of the eruption (Figure 7). Eruption onset is characterized by high temperature and high velocities. Acoustic power and liquid to condensed steam ratios do not peak at the beginning of the eruption, but rather exhibit longer period (minute-scale) unsteadiness for the first 4–5 min of the eruption. Maximum FLIR temperature is 86°C, which provides a lower bound on maximum temperature in the jet due to steam obscuring the jet core (boiling temperature is 93°C at the elevation of Lone Star). It is possible that lower than boiling temperatures reflect dissolved CO_2 in geyser waters [*Hutchinson et al.*, 1997] but this is unlikely because
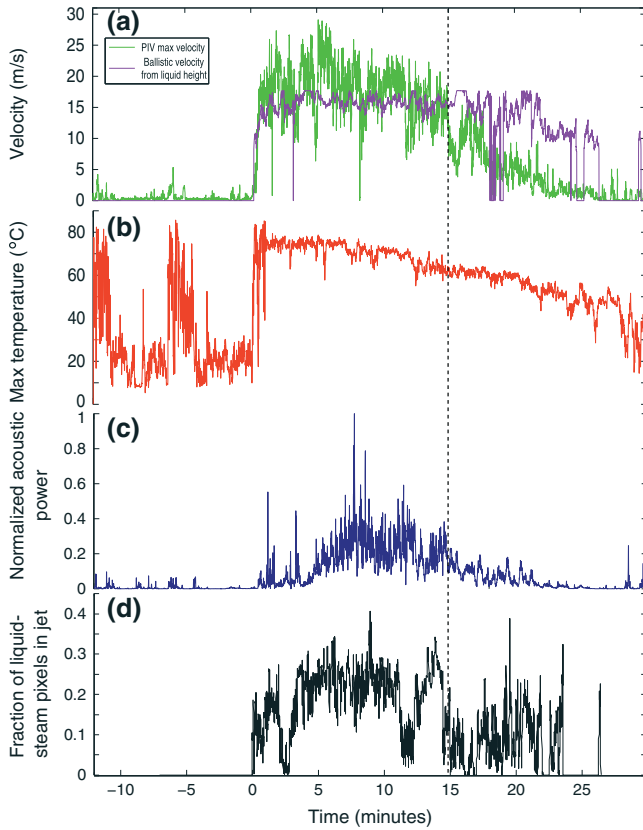
Figure 7. Comparison of (a) velocity time series from PIV (maximum value per frame) and from ballistic calculations. Note clipping in eruption column height for ballistic estimates. These represent upper and lower bounds for maximum jet velocity. (b) Maximum FLIR temperature, (c) acoustic power, and (d) fractions of liquid-steam dominated pixels region in jet. Time is zero at 15:15:41 UTC 23 September 2010. Dashed vertical line is inferred transition to steam dominated eruption.

the amount of CO_2 in thermal features near Lone Star is small [*Bergfeld et al.*, 2011].

[20] Maximum PIV velocity is 10–28 m s^{-1} in the first phase of the eruption, and maximum ballistic velocity based on liquid dominated jet height is ∼16 m s^{-1}. Throughout this phase, high-frequency variations in velocity and temperature are superimposed on a gradually declining maximum temperature. We also observe unsteady flow with a prominent 20 s period in PIV velocity and acoustic time series through this portion of the eruption (Figure 8). After 4–5 min of unsteadiness, acoustic power and liquid to condensed steam ratios remain high for roughly 8–10 min, making this the most steady portion of the main eruption.

[21] After ∼15 min of eruption, maximum velocities drop to 5–10 m s^{-1}, the amplitude of acoustic emissions drops, high frequency oscillations cease, and the period of low frequency oscillations in the flow increases to 30–40 s (Figure 8). This transition corresponds to a 50% drop in the percentage of liquid-steam pixels in visible video images, although the erupting column height remains high (∼11–14 m, seen in velocity estimate comparison of Figure 7). We interpret this transition as the onset of steam-dominated flow, following the peak in acoustic power that likely signals the beginning of steam fraction increase (acoustic noise depends both on fluid velocity and steam fraction). Jet velocity, temperature, and eruptive products become more variable in the last 5–10 min of the eruptions, gradually declining in magnitude until the jet is inactive and the eruption ends (Figure 7).

4.3. PIV Discharge Estimates

[22] To complement the direct measurement of discharge in the geyser outflow channels, we estimate the total discharge from our time series of jet velocity measurements. Our PIV calculations are not reliable enough to provide the complete velocity vector field through time, because water droplets obscure the jet core. Sensitivity analysis shows that PIV velocities likely overestimate true velocities by 5–10 m s^{-1} (supporting information). We therefore use both maximum PIV velocity estimates and ballistic calculations based on measured height of the liquid-dominated jet (Figure 7a) to compute total discharge. With these as maximum jet centerline velocities, we assume that the flow is well described by a fully developed, turbulent round jet which exhibits a self-similar velocity profile [*Pope*, 2000]

$$u_{\text{jet}} = u_{\text{max}} e^{-r^2/2\sigma^2}, \qquad (3)$$
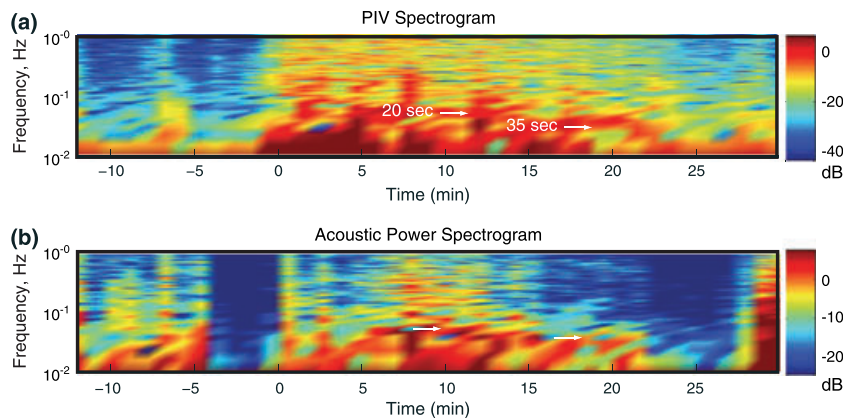

Figure 8. Spectrograms of (a) maximum PIV velocity and (b) acoustic emissions. The time period (and time interval plotted) is the same as in Figure 7. White arrows show dominant long-period variability in the data.
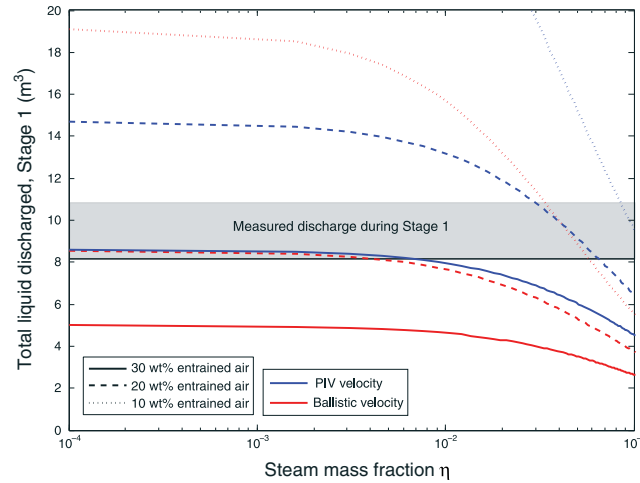
Figure 9. Calculated water discharge during the liquid-dominated phase (Phase 1) of Lone Star eruptions, as a function of erupting steam mass fraction. Water discharge is based on jet velocities determined by ballistic calculations (red curves) and PIV (blue curves) for vent radii of 0.2 m. Mass flux is corrected for the volume fraction of liquid calculated using equations (4) and (5). Solid and dashed curves are different choices for entrained air mass fraction, while the shaded bar is the range of main eruptive phase volumes observed. The horizontal solid line represents water discharge during the main phase of eruption 23 (8.1 m^3, supporting information).

with u_{max} the maximum centerline velocity, and r is a radial distance from the jet centerline. $2\sigma = x/5$ is the half width of the jet as a function of centerline distance from the vent x, which arises from the self-similar opening angle of fully turbulent axisymmetric jets. This formula does not describe compressible flows that exhibit supersonic expansion from the vent [*Chapman*, 2000]. It also neglects wind shear, buoyancy, and condensation effects. However, equation (3) provides a simple approximation that is consistent with the coarse scale of our velocity measurements. Our PIV region of interest extends 1–3 m above the vent (we use the average of $x = 1$ m in our calculations as maximum velocities per frame generally appear close to the vent). Equation (3) is integrated over the vent radius to calculate water discharge. We thus neglect possible residual ponding of water from previous eruptions on the cone in our discharge estimates.

[23] Both PIV and ballistic estimates must be corrected to account for the fact that the erupting fluid is a mixture of liquid and steam, plus entrained ambient air above the geyser vent. We assume that the vapor present in the jet is a linear mixture of air at ambient temperatures and steam at 93°C, then assume a mass fraction μ_{ent} of entrained air and calculate the volume of liquid discharged from the geyser Q_{liq} as

$$Q_{liq} = \mu_{ent} Q_{total} V_{liq}, \qquad (4)$$

where Q_{total} (m^3 s^{-1}) is the total (mixture) volume flux from the geyser scaled by the difference between pure steam and steam plus ambient air densities (a small correction as both hot steam and ambient air have low densities). V_{liq} (m^3) is the volume fraction of liquid, calculated as

$$V_{liq} = \frac{(1-\eta)/\rho_l}{(1-\eta)/\rho_l + \eta/\rho_g}. \qquad (5)$$

ρ_l, ρ_g (kg/m^3) are the densities of erupting H$_2$O liquid and steam, respectively, at 93°C and η is the mass fraction of

steam. We do not know the volume fraction of steam plus air at the vent, but other parameters in this calculation are fairly well constrained. Thus, we use liquid discharge measurements made in the streams that drain the geyser cone to constrain the mass fractions of steam and entrained air. The result is displayed in Figure 9, with the range of discharge measured for the entire experiment (supporting information), and a line indicating the 8.1 m^3 measured for the eruption studied in detail (eruption 23). For a maximum vent radius of 0.2 m, the steam mass fractions required to match observations are small (less than $\sim$0.01 unless the entrained air mass fraction is $<$ 0.2, in which case steam fractions are $>\sim$0.1). The mass fractions of steam and entrained air vary over the eruption, so this is an upper bound estimate averaged over the high velocity phase of the eruption cycle. As discussed in the next section, entrained air mass fractions are likely $>$ 0.2, so steam mass fractions are likely less than $\sim$0.01.

5. Discussion

[24] Based upon our experimental results, we can evaluate several aspects of Lone Star Geyser eruption dynamics in the context of the three questions outlined in the introduction. We first characterize the eruption cycle, then constrain the conditions required for choked conditions and vent overpressure during the main eruptive phase. Finally, we assess the overall energy budget of the Lone Star Geyser and its significance in the context of other Yellowstone geysers and regional heat flow.

5.1. Flow Oscillations and Instabilities

[25] An eruptive cycle consists of fountaining and system drainage, relaxation toward ambient conditions, gradual reservoir filling, and episodic pistoning (preplay) of the fluid filled conduit system (phases 1–4 in Figure 3). Eruptions occur when the conduit is at least partially filled, as

evidenced by the coincident oscillatory IR and acoustic signals and surface discharge during preplay events. Preplay events in which rising fluid overtops the cone generate pressure perturbations that induce deeper boiling and ultimately trigger a main eruption [*Kieffer*, 1989]. Decompression from reduced static load eventually initiates boiling at depth, generating steam bubbles that decrease density of the water column. This sets off a chain reaction of upward acceleration and further depressurization. Two phase flow is impeded by mechanical effects (conduit constrictions [e.g., *White*, 1967; *Kieffer*, 1984]) and dynamic effects such as bubble interactions. Thus, conditions for emptying the geyser reservoir are determined by the spatial and temporal distribution of bubble nucleation, growth, coalescence, and cavitation, and the geometry of Lone Star reservoir and conduit.

[26] Eruption proceeds until the available potential energy to drive flow is dissipated. The geyser plumbing system is not completely drained at this stage, as acoustic emissions indicate that subsurface liquid continues to boil vigorously. The upper conduit below the vent is, however, largely empty as evidenced by the lack of overtopping and the 8 s time lag in the IR and acoustic signals during these oscillations. Influx of fluid from a large reservoir at depth eventually serves to terminate these episodes (or else the geyser would become a fumarole) and the upper conduit fills gradually until preplay begins again.

[27] During all but phase 3 of the eruption cycle, we see long-period oscillatory flow signals (Figures 4, 5, and 8). The period and relative amplitude of these signals vary considerably throughout the eruption cycle, as does the relative phase of IR and acoustic oscillations (Figure 6). Short-period oscillations in jet velocity during the main eruptive phase also occur, although these are often obscured in video footage. The observed oscillatory flow signals likely correspond to boiling instabilities in the geyser plumbing system, consistent with descriptions of liquid and steam flow in tubes in applications ranging from boiling water nuclear reactors to refrigeration [*Boure et al.*, 1973; *Kakac and Bon*, 2008].

[28] Pressure-drop instabilities occur when a pressurized fluid flows from a pipe into a compressible chamber, often termed a surge tank in engineering applications [*Stenning*, 1964; *Kakac and Bon*, 2008]. Under a restricted range of parameter values that define this flow system, discharge increases when the pressure drop from inlet to outlet decreases. Similar flow instabilities occur also during lava dome growth and eruption [*Voight et al.*, 1999; *Denlinger and Hoblitt*, 1999; *Kozono and Koyaguchi*, 2012]. Water boiling at constant pressure in a compressible reservoir generates flow oscillations with periods ranging between 15 and 70 s, depending on heating rate, mass flux, and system geometry [*Kakac and Bon*, 2008]. The observed long-period oscillations at Lone Star Geyser are within this range. Models predict that longer periods of oscillations could result from either larger fluid or reservoir compressibility, or from decreasing the mass flow rate through the system, or by decreasing inlet fluid temperature [*Chiapero et al.*, 2012]. During the main eruption phase at Lone Star, gradual drainage and increased compressibility (increasing steam fraction) in the subsurface reservoir are consistent with the observed long-period pressure-drop oscillations. Oscillations during the posteruption relaxation and preplay phases have similar order of magnitude periods that

also increase with time, but occur during periods when mass flow rate in the plumbing system is lower. During these phases, pressure-drop instabilities could be consistent with the observations if fluid pressure in the deeper part of the system remains high and inlet fluid temperature remains constant.

[29] The instabilities observed during the relaxation and preplay phases (phases 2 and 4) could be explained by mechanisms other than pressure drop, such as steam-chugging instabilities in a partially filled system [e.g., *Pitts*, 1980] multi-channel flow instabilities [*Kakac and Bon*, 2008], or density wave instabilities for short-period oscillations [*Fujita et al.*, 2011]. Nevertheless, the coincidence between acoustic and IR signals during the preplay phase indicates that much of the boiling occurs near the ground surface (Figure 6a). Perturbations of the pressure profile caused by fluid discharge modulate mass flux and could drive pressure-drop instabilities, and this pressure perturbation ultimately triggers an eruption. In contrast, the 8 s lag between the acoustic and IR signals during the posteruption relaxation phase Figure 6b, likely reflects boiling deeper in the flow system (Figure 4). Speeds of buoyantly rising steam are 2–3 orders of magnitude smaller than steam sound speeds (Figure 10a), thus rise times of steam driven off of an oscillating boiling interface are quite reasonably ~8 s longer than acoustic travel times for a ~10 m conduit.

5.2. Choked Flow at Lone Star Geyser

[30] Some geyser (as well as volcanic) eruptions likely exhibit choked, or supersonic, flow [e.g., *Kieffer*, 1989]. This condition occurs when the flow Mach number $M = u/c \geq 1$, where u is the flow velocity and c the sound speed of the liquid-vapor mixture [*Kieffer*, 1977]. The choke point is a constriction which defines the narrowest part of the conduit. Subsonic or supersonic flow downstream of the constriction largely depends on vent geometry, the sound speed of the liquid-steam mixture, and fluid overpressure upstream of the constriction [e.g., *Chapman*, 2000; *Koyaguchi et al.*, 2010]. When the flow is choked, pressures upstream and downstream of the constriction are not in equilibrium.

[31] Choked flow could be unsteady downstream of the choke point for overpressured jets. Additionally, the sound speed itself of liquid-steam mixtures is a strong function of steam mass fraction, which varies during the eruption. At 100 °C and 1 bar, sound speed can vary from 1545 m s^{-1} for pure liquid water to ~1 m s^{-1} for very small steam mass fractions at thermodynamic equilibrium with the liquid. The sound speed for pure steam at 100°C and 1 bar is 472 m s^{-1} [*Kieffer*, 1977]. Sound speeds under thermodynamic equilibrium and nonequilibrium conditions differ by as much as an order of magnitude for a given mass fraction of steam [*Kieffer*, 1977]. Derivation of liquid-steam sound speed formulae for both equilibrium (mass exchange between liquid and vapor phase occurs is rapid on time scales of interest, with negligible momentum transfer between phases) and nonequilibrium cases is presented in Appendix A. Variation of steam fraction with time as observed during geyser eruptions implies strongly variable sound speeds (Figure 10a), but it remains to be demonstrated that the measured jet velocities equal the sound speed, indicating that the flow is choked.
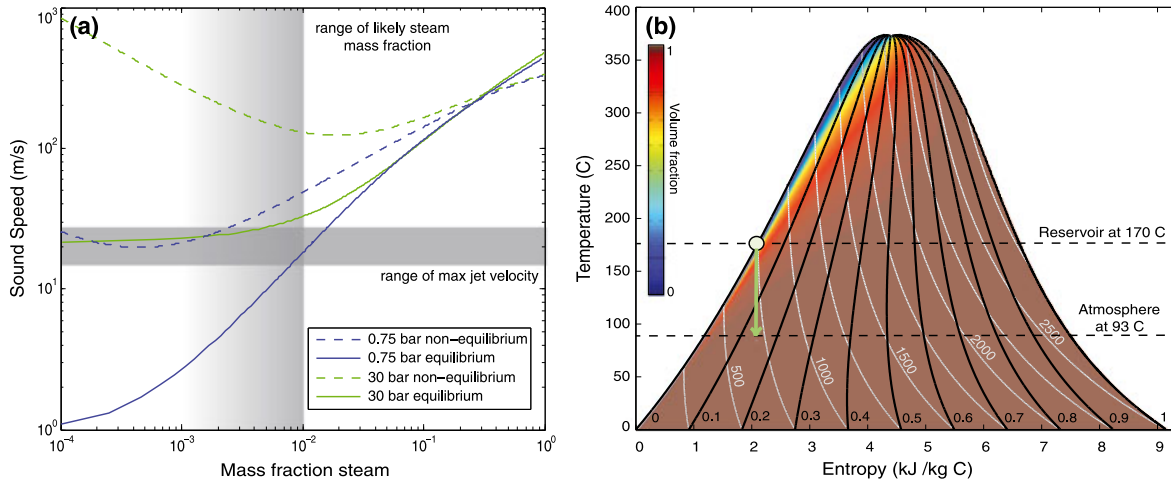
Figure 10. (a) Sound speed of equilibrium and nonequilibrium liquid-steam mixtures (equations in Appendix) for two end-member vent pressure values. Horizontal gray shading indicates bounds on maximum measured velocity from video footage. The vertical gray bar is our preferred range of steam mass fraction based on discharge measurements. (b) Temperature-entropy phase diagram for pure water. Dark curves represent mass fraction of steam, light curves isenthalps, coloring is volume fraction of steam. Isentropic decompression pathway from the upper bound on reservoir temperature based on geothermometry to the surface is shown by the green arrow.

[32] The absolute fraction of steam and its variation with time are not well constrained by our measurements. However, we have direct measurements of jet velocity, a relative measure of liquid to condensed steam, and a geochemically-derived subsurface reservoir temperature that allow us to estimate the steam fraction over an entire eruption cycle. Because a significant amount of work is consumed by the fluid during the expansion of a liquid into a liquid-steam mixture, we follow the approach of *Kieffer and Delany* [1979] and *Kieffer* [1989], assuming isentropic (rather than isenthalpic) decompression of the 160–170°C reservoir liquid (section 4.1) to the ground surface where the boiling temperature is 93°C. This isentropic decompression generates 11.5–13.0 wt % steam at the surface (Figure 10b). The calculated sound speeds in both equilibrium and nonequilibrium cases for this steam mass fraction are more than an order of magnitude greater than jet velocities measured by video. Isenthalpic or irreversible decompression [*Thiery and Mercury*, 2009] would lead to even larger fractions of steam and sound speeds at the surface (the path of gray isenthalps from reservoir temperature to atmosphere in Figure 10b rather than a vertical isentrope). These conditions would be even less favorable for choked flow over any part of the eruption cycle.

[33] Matching of the calculated and observed geyser discharge during the main eruption phase (Figure 9) suggests that the mass fraction of steam at the vent is considerably less when entrainment of ambient air is accounted for. Entrainment of ambient air (μ_{ent}) can be estimated through simplified models for jet flow such as Plumeria [*Mastin*, 2007], that solve one-dimensional equations for mass, momentum, and energy for wet volcanic plumes. For example, for a vent radius of $r = 0.15$ m, exit velocity of 15 m s^{-1}, water temperature 100°C, and a steam mass fraction of 0.06, the mass fraction of entrained air is $\sim$0.25–0.50 at distances of 1–3 m from the vent using Plumeria calculations. The entrainment coefficient in Plumeria is 0.09,

which may overestimate the entrainment rate in the near-vent region (L.G. Mastin, U.S. Geological Survey, 2015, written communication). Experimental studies suggest that for choked and overpressured jets, air mass fractions are in the range of $\sim$0.15–0.25 at distances of 5–10 vent diameters from the vent orifice [*Solovitz et al.*, 2011]. We thus infer that entrained air can account for at least 0.20–0.25 by mass of the Lone Star jet.

[34] Assuming $\mu_{ent} = 0.20$, the maximum steam mass fraction is between 0.005 and 0.06 for lower (ballistic) and upper (PIV) bounds on discharge, respectively (Figure 9). Lower bounds on steam mass fraction are not as well constrained, but could be even lower than 10^{-3} if $\mu_{ent} > 0.3$. Because these estimates of steam mass fraction assume the largest reasonable vent radius (0.2 m), steam mass fractions are likely ≥ 0.01.

[35] The maximum measured jet velocities that range between 16 and 28 m s^{-1} (Figure 7) are similar to the calculated sound speeds for nonequilibrium (20–40 m s^{-1}) and equilibrium (1–20 m s^{-1}) conditions for steam mass fractions of ≤ 0.01 at 0.75 bar (horizontal gray bar in Figure 10a). Choking of the jet most likely occurs during the steady portion of the eruption (minutes $\sim$3–12 in Figure 7), before steam fractions become large. Because of the large volume expansion incurred by small fractions of steam (coloring in Figure 10b), it is plausible that sound speed velocities could be reached at shallow depth. This is consistent with a constriction at a depth of $\sim$7 m in the Old Faithful geyser conduit that was proposed to be a choke point [*Hutchinson et al.*, 1997].

5.3. Vent Fluid Overpressure

[36] Following the analysis of *Koyaguchi et al.* [2010], for a Lone Star conduit with radius 0.1–0.2 m, the choke point will occur in the subsurface if we assume that the flow is choked. If the upstream fluid pressure is greater than ambient pressure (overpressured), then the flow will expand when
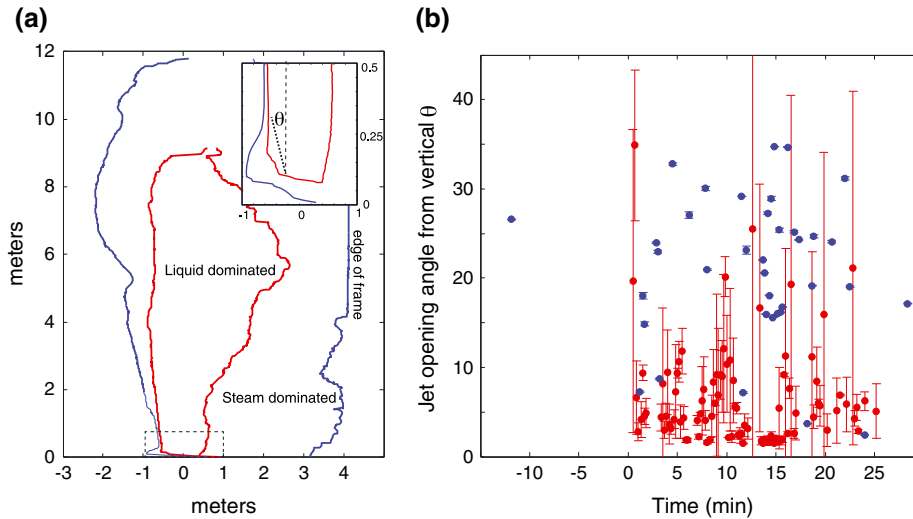
Figure 11. (a) Outlines of liquid and steam dominated regions of the jet during the main eruption phase. Inset shows the region over which the jet exit angle is measured. (b) Time series of exit angle for the left-hand side of the jet in Figure 11a during the eruption. Colors correspond to labels in Figure 11a, points are averages over 30 s windows, with a 1σ error.

exiting from the vent, equilibrating with the atmosphere via Prantl-Meyer expansion and a series of shocks [*Kieffer*, 1984; *Chapman*, 2000]. In contrast, under-pressured eruption columns (pressure at the top of the vent region is lower than atmospheric) will curve inward and narrow above the vent rim. We use image processing results to estimate the near-vent angle of the liquid-dominated region in the jet. The area ~10 cm directly above the cone is obscured by steam and by small secondary vents (Figure 11a). Therefore, we concentrate on a region of 0.1–0.3 m above the vent where wind effects are minimal. For this region, we fit a straight line to the endpoints of the jet margin defined by the lateral boundary between the liquid and steam dominated fields (Figure 11a). We constrain the bottom end of this boundary to 0.2 m from the center of the jet (maximum estimated vent radius) and 0.1 m above the vent (where the jet appears above spray from minor vents, inset in Figure 11a). Taking a top endpoint of this interface 0.3 m above the vent (1.5–3 vent diameters), this boundary segment provides a minimum measure of the expansion angle for both liquid and condensed steam dominated pixels in video frames. A top boundary of >0.3 m above the vent, or a vent radius <0.2 m, results in larger opening angles but the overall trends remain similar. We calculate the expansion angle at 3 Hz throughout the main eruptive phase.

[37] Results are shown in Figure 11b, for regions in the jet dominated by liquid and by condensed steam. We have taken a 30 s window to find the running average and standard deviation of jet angle from the vertical and eliminated outliers whose angle is > 45°C. The jet is close to vertical for the main eruptive phase but it expands away from the vent, indicating that the flow is overpressured. In the last 10–15 min of the eruption, the opening angle appears to increase in magnitude and variance, and air entrainment and buoyancy are more significant.

[38] Mach disks, which are under expanded regions expected from choked flow [*Addy*, 1981], are not observed in the visible video. We therefore calculate vent overpres-

sure by measuring maximum jet expansion using the relation [*Ogden et al.*, 2008]:

$$K = (r_m/r_v)^2, \tag{6}$$

where K is the ratio of vent pressure to atmospheric pressure, r_v (m) is vent radius, and r_m is maximum jet radius. There calculations neglect steam condensation, plume buoyancy, and wall friction. In addition, Lone Star Geyser does not scale geometrically to the numerical simulations performed by *Ogden et al.* [2008]. During the first 15 min of eruption phase 1, the mean value of maximum liquid-dominated width in the bottom 30 cm of the jet is 0.79 m. Using a vent radius of 0.2 m, and assuming that r_m equals to the width of the liquid-dominated jet (an upper bound), we find an overpressure ratio of 15.6, implying a vent exit pressure of 1.2 MPa. This is an upper bound on vent exit fluid pressure, given the neglect of buoyancy and condensation and coarse scale method for determining jet width. Calculations with a vent radius of 0.1 m result in an overpressure of 4.9 MPa, which we consider to be less realistic as it is comparable to the tensile strength of rock. If choked flow conditions persist at the vent and the flow is in thermodynamic equilibrium, the largest possible vent pressure is ~2 MPa. Calculated nonequilibrium sound speeds do not match well with the data (Figure 10a).

5.4. Geyser Energetics and Heat Output

[39] We calculate the heat output (power) of Lone Star Geyser by assuming that 11.5–13.0 wt % steam (section 5.2) and liquid cool from 93°C (boiling temperature) to ambient, which at Yellowstone is ~0°C on average. To calculate the heat transported by liquid water, we multiply the measured average water volume erupted during an eruption cycle (21 m^3) by water density at 93°C (963 kg m^{-3}) and divide by average eruption duration (3 h) to obtain an average mass flow rate of 1.9 kg s^{-1}. Multiplying this flow rate by liquid enthalpy at 93°C (390 kJ kg^{-1}) results in a total output of

0.72 MW. The heat transported by 11.5 wt % and 13.0 wt % steam (enthalpy of 2665 kJ kg^{-1} at 93°C) amounts from 0.64 MW to 0.74 MW, respectively. Thus, despite the relatively small amount of steam discharge, heat transported by steam accounts from 47% to 51% of the geyser's total heat output, 1.4–1.5 MW. The calculated heat output is an order of magnitude greater than that estimated by other means for Old Faithful geyser [*Rinehart*, 1980, p.61], but is only a very small fraction of the minimum heat flow estimate (4 GW) from the Yellowstone Caldera [*Hurwitz et al.*, 2012b]. This suggests that even if all of the ∼500 geysers in Yellowstone would have the same output as Lone Star, their contribution to the heat output from the Yellowstone Caldera would be small.

[40] The average kinetic energy (E_k) available to lift the jet during the entire 3 h eruption cycle can be calculated from the enthalpy difference between the 160–170°C liquid and the 93°C two-phase mixture containing 11.5–13.0 wt % steam. Using the relation $E_k = 1/2 \, m \, u_t^2$ with m water mass and u_t average rise velocity, the calculated enthalpy difference of 24–34 kJ/kg and a mass flow rate of 2 kg/s (measured water discharge divided by an eruption cycle lasting 3 h) results in velocities of 7–8 m s^{-1}. These velocities are obviously lower than values estimated from PIV, as they are averages over different time scales; subsecond for the PIV and approximately 3 h represented by these calculations. Energy release is not uniform in time: the declining ratio of liquid to steam in the erupting jet implies that much of the energy release occurs in the first 15 min of eruption.

6. Conclusions

[41] Our study of Lone Star Geyser provides one of the most detailed characterization of a geyser eruption column to date, a well constrained estimate of erupted volume and an energy budget for a large geyser. Our experiment reaffirms the consistency of Lone Star eruptions within the 5 days of experiment, with four clear phases of eruption reflected in erupting volume as well as IR signals and acoustic emissions (Figure 3). Our findings of long-period oscillatory signals during the main eruption as well as during the posteruption relaxation phase and preplay suggest that boiling instabilities play a fundamental role in geyser eruptions. We find that dominant periods of oscillation range from 20 to 70 s, with gliding periods during the relaxation and preplay eruptive phases (Figure 4). In particular, we suggest that pressure-drop instabilities involving a compressible subsurface reservoir along the flow path explain these oscillations.

[42] A transition from liquid to steam dominated flow corresponds to an increase in the unsteadiness of flow (Figure 7 and 8), suggesting that emptying or increased compressibility in the reservoir controls time variation of discharge during phase 1 of the geyser eruption. We provide a well constrained erupted volume from all phases of the eruption cycle at a large geyser (supporting information) and use these measurements to constrain steam fraction during the main eruptive phase (Figure 9). We estimate steam mass fractions of < 0.01 for this stage, which likely makes Lone Star eruptions choked during the main eruptive phase, the choke point being a conduit constriction at depth. Based on jet opening angle, we broadly bound vent overpressure of < 3 MPa, which is consistent with choked flow under near-equilibrium conditions. Finally, we use chemical geothermometry to estimate a reservoir temperature of 167–190°C and total heat output for an eruption cycle (1.4–1.5±0.4 MW).

Appendix A: Sound Speeds in Liquid Vapor Mixtures

[43] To calculate the sound speed of fluid in the Lone Star geyser, we implement the model of *Kieffer* [1977], which derives sound speed for the case in which both phases are in thermodynamic equilibrium, and the case of adiabatic, nonequilibrium sound speed. This model is reproduced in *Lu and Kieffer* [2009]. Unfortunately, a number of typographical errors in *Kieffer* [1977] make it difficult to reproduce the results (the figures, however, are correct in that work). This has been recognized and corrected for in the nonequilibrium case by *Kumagai and Chouet* [2000] and *Morrissey and Chouet* [2001]

$$c_{ne} = \left(C_0 + \exp\left(\frac{P_r - P}{K}\right)\right)\left[\sqrt{(1+\eta)\rho_{lr}}\sqrt{\frac{C_0}{\gamma P} + \frac{1}{K}\exp\left(\frac{P_f - P}{K}\right)}\right]^{-1} \quad (A1)$$

as the sound speed under the adiabatic assumption and appropriate for gas volume fractions in the range of 10–90%. Here $C_0 = \eta\rho_{lr}(G/P)^{1/\gamma}$, $G = TR/\rho_g^{\gamma-1}$, and $\rho_g = P/(RT)$. ρ_{lr} is the density of pure liquid at reference pressure $P_r = 1$ bar, γ is the heat capacity ratio, K is the bulk modulus of the liquid, T is the temperature, P is the pressure, and η is the mass fraction of gas.

[44] For completeness, we reproduce the derivation of equilibrium sound speed from *Kieffer* [1977] in full here. Thermodynamic equilibrium in multiphase systems requires that mass transfer occurs between phases more rapidly than the acoustic wave period. Equilibrium sound speed c_e is then calculated assuming that both the entropy and volume fraction of all phases remain constant. We restrict to two phases and the small pressure limit here; a more general treatment of this calculation for arbitrary number of phases is given in *Castier* [2011].

[45] Following *Kieffer* [1977], an adiabatic change in volume of the mixture is, for specific volume v

$$dv = \left(\frac{\partial v}{\partial P}\right)_{S,\eta} dP + \left(\frac{\partial v}{\partial \eta}\right)_{P,S} d\eta, \quad (A2)$$

from which we find the sound speed c_e

$$-\left(\frac{v}{c_e}\right)^2 = \left(\frac{\partial v}{\partial P}\right)_S = \left(\frac{\partial v}{\partial P}\right)_{S,\eta} + \left(\frac{\partial v}{\partial \eta}\right)_{P,S}\frac{d\eta}{dP}. \quad (A3)$$

Here P is pressure, η is mass fraction steam, and S is specific entropy. In the small pressure limit $(\partial v/\partial\eta)_{P,S} \approx v_g - v_l$, the difference in specific volumes of saturated vapor and liquid specific volumes. We can then split up the system derivative of volume component-wise (l, g are liquid and gas)

$$\left(\frac{\partial v}{\partial P}\right)_{S,\eta} = (1-\eta)\left(\frac{\partial v_l}{\partial P}\right)_{\text{sat}} + \eta\left(\frac{\partial v_g}{\partial P}\right)_{\text{sat}}. \quad (A4)$$

Invoking the first law of thermodynamics relating total energy Q to work and internal energy E, and an adiabatic change

$$\delta Q = 0 = \delta E + P\delta v = \delta H - v\delta P, \quad (A5)$$

where we have used the specific enthalpy of reaction δH in place of δE.

[46] Again splitting into components and assuming saturation values, we have

$$H = (1 - \eta)H_l + \eta H_g = H_l + \eta L \tag{A6}$$

and

$$\delta H = \delta H_l + \eta \delta L + L \delta \eta, \tag{A7}$$

where L is the latent heat of vaporization.

[47] Rearranging terms and using equation (A5), we have

$$\left(\frac{\delta \eta}{\partial P}\right)_S \approx \left(\frac{\partial \eta}{\partial P}\right)_S = \frac{v}{L} - \frac{1}{L}\left(\frac{\partial H_l}{\partial P}\right) - \frac{\eta}{L}\left(\frac{\partial L}{\partial P}\right). \tag{A8}$$

[48] The equilibrium sound speed then follows from inserting equations (A8) and (A4) into the definition of sound speed, using saturation values for each phase

$$c_e^2 = -v^2 \left((1 - \eta)\left(\frac{\partial v_l}{\partial P}\right) + \eta \left(\frac{\partial v_g}{\partial P}\right)\right.$$
$$\left. + (v_g - v_l)\left[\frac{v}{L} - \frac{1}{L}\left(\frac{\partial H_l}{\partial P}\right) - \frac{\eta}{L}\left(\frac{\partial L}{\partial P}\right)\right]\right)^{-1}. \tag{A9}$$

[49] We use steam tables to compute the four needed partial derivatives of thermodynamic variables numerically. A Matlab script to calculate both equilibrium and nonequilibrium sound speeds is available upon request to the authors.

Appendix B: Experimental Methods

[50] In what follows, we present a more detailed explanation of experimental methods and instrumentation. For locations, refer to the map (Figure 1b). Eruption times were determined using three Infrared (IR) sensors (Electro Optical Systems Model TP-020-HTELE) connected to a simple Keplerian telescope with an aperture of 25.4 mm and f-ratio of 1. The IR sensor operates at wavelengths of 7–18 μm. The IR sensors were connected to data loggers with a GPS clock with data sampling at 0.5 Hz.

[51] Video was acquired during nine eruptions at visible (Canon Vixia HF-S100, 30 frames/s and 540 by 960 pixel) and infrared (FLIR A320 camera, 320 by 240 pixel frames, ∼15 fps) wavelengths. We set up a GRAS microphone (3 Hz–20 kHz) with a flat frequency response and a sensitivity of 40mV/Pa at a distance of 20 m from the cone. Acoustic signals were recorded on a Guralp DM24 digitizer with a preamplifier at a rate of 1000 Hz. We also made several acoustic measurements using a portable recorder at 44100 Hz [H2, Zoom Company].

[52] We estimated the volume of liquid water discharged from the geyser for each period of the eruption cycle by making stream flow measurements along two of the three main geyser outflow channels for eight eruption cycles. We deployed a pressure transducer (0.5 Hz sample rate) in each of the two channels and established rating curves by measuring the depth of small pools for the entire range of water flow in the channel (supporting information). Water velocity was measured with a video camera (30 fps) using a floating marker, such as a bubble or a wood chip, over a measured distance. We obtained discharge estimates for each stream by measuring the average cross-sectional area of the two channels and multiplying by water velocity. Flow in the middle stream, which is much lower than the other two streams, is

Table B1. Mean and Standard Deviation Intensity Values for Mahalonobis Image Segmentation [*Gonzalez et al.*, 2004]

	Liquid-Steam Region	Condensed Steam-Air Region
RGB Mean Λ	208.827	164.664
	199.967	158.394
	198.236	162.023
Std. Dev.	18.122	21.328

estimated by spot measurements and comparison with the other two streams. Base flow from small springs near the geyser is estimated during noneruptive periods, and durations of increased discharge are also estimated (supporting information).

[53] On 8 April 2012, we returned to Lone Star Geyser to collect water samples during a single eruptive cycle from the two main channels draining the geyser. Six water samples were collected from the east channel and four samples were collected from the west channel (Figure 1b, supporting information). One sample was taken from a spring near the cone. The samples were analyzed for their major element chemistry (supporting information) at the U.S. Geological Survey laboratories in Boulder, Colorado and Menlo Park, California following analytical procedures described in *Ball et al.* [2010] and *Hurwitz et al.* [2012b].

B1. Video Image Processing

[54] We obtain estimates of the velocity distribution within the erupting column by performing particle image velocimetry (PIV) processing of visible video frames, using the Matlab based OpenPIV software (http://www.openpiv.net). PIV is a cross-correlation method performed on tiled windows between successive video frames. We use a Region of Interest (ROI) window size of 32 horizontal by 128 vertical pixels, tiled with an eight pixel offset, in the near-vent region of the jet (example in Figure 2a), with the OpenPIV signal to noise parameter set to 5. Resolution tests (supporting information) were performed to ensure that the ROI was large enough to capture particle movement frame-to-frame. We find that a ROI height of 128 pixels is sufficient to consistently capture particle movement frame-to-frame, and that larger windows do not significantly change the results. Errors in maximum PIV velocity estimates per frame are larger than mean velocity per frame. Based on the total variance between ROI window sizes that yielded similar velocities for a 1 s sample within error, we estimate that PIV maximum velocity magnitudes may have up to 5–10 m s^{-1} error, while mean velocity magnitudes are only 1–2 m s^{-1}.

[55] Visible video offers the opportunity to quantify the variable amounts of steam and liquid that erupt, given the color contrast between condensed steam-air (droplets in air) and liquid-steam (bubbles in liquid) mixtures. Although it is not possible to directly quantify liquid/steam fractions in this manner, we can clearly distinguish color differences between regions with liquid-steam mixtures and more dilute and transparent condensed steam-air mixture regions. We use this method to estimate liquid-dominated jet height and relative liquid to steam ratios through the eruption.

[56] To automate the segmentation of these regions through time, we use a common image processing technique

on RGB frames, the Mahalonobis distance [*Gonzalez et al.*, 2004], defined as

$$d_M = (\mathbf{X} - \mathbf{\Lambda})S^{-1}(\mathbf{X} - \mathbf{\Lambda}), \tag{B1}$$

where $\mathbf{X}$ is the three channel Red Green Blue (RGB) color vector at each pixel in the image, $\mathbf{\Lambda}$ is a vector of mean values of the RGB range of interest, with S the covariance matrix of this reference range. We find the reference values for the "liquid-steam" and "steam-air" regions through machine learning. We manually selected these regions from a training set of 30 images smoothed with a 20 pixel window drawn at random from the main eruption and used these to compute $\mathbf{\Lambda}$ and S for each (Table B1). We experimented with different numbers of training images without a significant effect on the final results. We then compute the Mahalonobis distance for the entire eruption subsampled at 3 Hz, assigning each pixel to a class ("liquid-steam", "steam-air", "other", Figure 2b) if the d_M lies within 1 standard deviation of the mean for that class.

References

Addy, A. (1981), Effects of axisymmetric sonic nozzle geometry on Mach disk characteristics, *AIAA J.*, *191*, 121–122.

Ball, J., R. McCleskey, and D. Nordstrom (2010), Water-chemistry data for selected springs, geysers, and streams in Yellowstone National Park, Wyoming, 2006–2008, *Open-File Report 2010-1192*, U.S. Geological Survey.

Belousov, A., M. Belousova, and A. Nechayev (2013), Video observations inside conduits of erupting geysers in Kamchatka, Russia, and their geological framework: Implications for the geyser mechanism, *Geology*, *41*(7), doi:10.1130/G33366.1.

Bergfeld, D., J. Lowenstern, A. Hunt, W. Shanks, and W. Evans (2011), Gas and isotope chemistry of thermal features in Yellowstone National Park, Wyoming, *US Geological Survey Scientific Investigative Report, 2011–5012*.

Boure, J., A. Bergles, and L. Tong (1973), Review of two-phase flow instability, *Nucl. Eng. Des.*, *25*(2), 165–192.

Brilliantov, N., J. Schmidt, and F. Spahn (2008), Geysers of Enceladus: Quantitative analysis of qualitative models, *Planet. Spac. Sci.*, *56*, 1596–1606.

Bryan, T. (1995), *The Geysers of Yellowstone*, Univ. Press of Colorado.

Bunsen, R. (1847), Physikalische beobachtungen uber die hauptsachlichsten geysir islands, *Ann. Phys. Chem.*, *83*, 159–170.

Castier, M. (2011), Thermodynamic speed of sound in multiphase systems, *Fluid Phase Equilib.*, *306*, 204–211.

Chapman, C. (2000), *High Speed Flow*, vol. 258, Cambridge University Press, New York, NY.

Chiapero, E., M. Fernandino, and C. Dorao (2012), Review on pressure drop oscillations in boiling systems, *Nucl. Eng. Des.*, *250*, 436–447.

Crone, T., R. McDuff, and W. Wilcock (2008), Optical plume velocimetry: A new flow measurement technique for use in seafloor hydrothermal systems, *Exp. Fluids*, *45*(5), 899–915.

Denlinger, R., and R. Hoblitt (1999), Cyclic eruptive behavior of silicic volcanoes, *Geology*, *27*, 459–462.

Fournier, R. (1969), Old Faithful: A physical model, *Science*, *163*, 304–305.

Fournier, R. (1979), A revised equation for the Na/K geothermometer, *Geotherm. Resour. Counc. Trans.*, *3*, 221–224.

Fournier, R. (1981), Application of water geochemistry to geothermal exploration and reservoir engineering, in *Geothermal Systems: Principles and Case Histories*, edited by L. Ryback, and L. Muffler, pp. 109–143, Wiley, New York.

Fournier, R., and R. Potter (1982), An equation correlating the solubility of quartz in water from 25° to 900°c at pressures up to 10,000 bars, *Geochim. Cosm. Act.*, *46*, 1969–1973.

Fournier, R., and J. Rowe (1966), Estimation of underground temperatures from the silica content of water from hot springs and wet-steam wells, *Am. J. Sci.*, *264*, 685–697.

Fujita, E., K. Araki, and K. Nagono (2011), Volcanic tremor induced by gas-liquid two-phase flow: Implications of density wave oscillation, *J. Geophys. Res.*, *116*, B09201, doi:10.1029/2010JB008068.

Gonzalez, R., R. Woods, and S. Eddins (2004), *Digital Image Processing Using Matlab*, 1st ed., Pearson Prentice Hall.

Hurwitz, S., A. Kumar, R. Taylor, and H. Heasler (2008), Climate-induced variations of geyser periodicity in Yellowstone National Park, USA, *Geology*, *36*(6), 451–454.

Hurwitz, S., R. Harris, C. Werner, and F. Murphy (2012a), Heat flow in vapor dominated areas of the Yellowstone plateau volcanic field: Implications for the thermal budget of the Yellowstone caldera, *J. Geophys. Res.*, *117*, B10207, doi:10.1029/2012JB009463.

Hurwitz, S., A. Hunt, and W. Evans (2012b), Temporal variations of geyser water chemistry in the upper geyser basin, Yellowstone National Park, USA, *Geochem. Geophys. Geosyst.*, *13*, Q12005, doi:10.1029/2012GC004388.

Husen, S., R. Taylor, R. Smith, and H. Healser (2004), Changes in geyser eruption behavior and remotely triggered seismicity in Yellowstone National Park produced by the 2002 M 7.9 Denali Fault earthquake, Alaska, *Geology*, *32*(6), 537–540.

Hutchinson, R. (1985), Hydrothermal changes in the Upper Geyser Basin, Yellowstone National Park, after the 1983 Borah Peak, Idaho, earthquake, *Proceedings of Workshop XXVIII on the Borah Peak, Idaho, earthquake: USGS open–file report 85-0290-A*, pp. 612–624, Menlo Park, Calif.

Hutchinson, R., J. Westphal, and S. Kieffer (1997), In situ observations of Old Faithful Geyser, *Geology*, *25*, 875–878.

Ingebritsen, S., and S. Rojstaczer (1993), Controls on geyser periodicity, *Science*, *262*, 889–892.

Ingebritsen, S., and S. Rojstaczer (1996), Geyser periodicity and the response of geysers to deformation, *J. Geophys. Res.*, *101*, 891–905.

Jaggar, T. (1898), Some conditions affecting geyser eruption, *Am. J. Sci.*, *5*, 323–333.

Kakac, S., and B. Bon (2008), A review of two-phase flow dynamic instabilities in tube boiling systems, *Intern. J. Heat Mass Trans.*, *51*, 399–433.

Kedar, S., B. Sturtevant, and H. Kanamori (1996), The origin of harmonic tremor at Old Faithful Geyser, *Nature*, *379*, 708–711.

Kieffer, S. (1977), Sound speed in liquid-gas mixtures: Water-air and water-steam, *J. Geophys. Res.*, *8*(2), 2895–2905.

Kieffer, S. (1984), Seismicity at old faithful geyser; an isolated source of geothermal noise and possible analogue of volcanic seismicity, *J. Volcanol. Geotherm. Res.*, *22*, 59–95.

Kieffer, S. (1989), Geologic nozzles, *Rev. Geophys.*, *27*, 3–38.

Kieffer, S., and J. Delany (1979), Isentropic decompression of fluids from crustal and mantle pressures, *J. Geophys. Res.*, *84*, 1611–1620.

Koyaguchi, T., Y. Suzuki, and T. Kozono (2010), Effects of the crater on eruption column dynamics, *J. Geophys. Res.*, *115*, B07205, doi:10.1029/2009JB007146.

Kozono, T., and T. Koyaguchi (2012), Effects of gas escape and crystallization on the complexity of conduit flow dynamics during lava dome eruptions, *J. Geophys. Res.*, *117*, B08204, doi:10.1029/2012JB009343.

Kumagai, H., and B. Chouet (2000), Acoustic properties of a crack containing magmatic or hydrothermal fluids, *J. Geophys. Res.*, *105*(B11), 25493–25512, doi:10.1029/2000JB900273.

Leifer, I., and I. Macdonald (2003), Dynamics of the gas flux from shallow gas hydrate deposits: Interaction between oily hydrate bubbles and the oceanic environment, *Earth Planet. Sci. Lett.*, *210*, 411–424.

Lu, X., and S. Kieffer (2009), Thermodynamics and mass transport in multicomponent, multiphase H_2O systems of planetary interest, *Annu. Rev. Earth Planet. Sci.*, *37*(1), 449–477.

Mackenzie, G. (1811), *Travels in the Island of Iceland, Edinburgh*, vol. 27, Alam and Company, Edinburgh.

Mastin, L. (1995), Thermodynamics of gas and steam-blast eruptions, *Bull. Volcanol.*, *57*, 85–98.

Mastin, L. (2007), A user-friendly one-dimensional model for wet volcanic plumes, *Geochem., Geophys., Geosyst.*, *8*, Q03014, doi:10.1029/2006GC001455.

McCleskey, R., L. Clor, J. Lownstern, W. Evans, D. Nordstrom, H. Heasler, and M. Huebner (2012), Solute and geothermal flux monitoring using electrical conductivity in the Madison, Firehole,

and Gibbon rivers, Yellowstone National Park, *Appl. Geochem.*, *27*, 2370–2381.

Morrissey, M., and B. Chouet (2001), Trends in long-period seismicity related magmatic fluid compositions, *J. Volcanol. Geotherm. Res.*, *108*, 265–281.

Ogden, D., K. Wohletz, G. Glatzmaier, and E. Brodsky (2008), Numerical simulations of volcanic jets: Importance of vent overpressure, *J. Geophys. Res.*, *113*, B02204, doi:10.1029/2007JB005133.

Pitts, J. (1980), Steam chugging in a boiling water reactor pressure-suppression system, *Int. J. Mult. Flow*, *6*, 329–344.

Pope, S. (2000), *Turbulent Flows*, Cambridge University Press, Cambridge, U.K.

Porco, C., et al. (2006), Cassini observes the active south pole of Enceladus, *Science*, *311*, 1393–1401.

Rinehart, J. (1980), *Geysers and Geothermal Energy*, Springer-Verlag, New York.

Rudolph, M., M. Manga, S. Hurwitz, M. Johnston, L. Karlstrom, and C.-Y. Wang (2012), Mechanics of Old Faithful Geyser, Calistoga, California, *Geophys. Res. Lett.*, *39*, L24308, doi:10.1029/2012GL054012.

Sohn, R., R. Thompson, A. Rabinovich, and A. Mihaly (2009), Bottom pressure signals at the TAG deep–sea hydrothermal field: Evidence for short-period, flow-induced ground deformation, *Geophys. Res. Lett.*, *36*, L19301, doi:10.1029/2009GL040006.

Solovitz, S., L. Mastin, and F. Saffaraval (2011), Experimental study of near-field entrainment of moderately overpressured jets, *J. Fluid. Eng.*, *133*, 051304.

Steinberg, G. (1980), The enthalpy of the heat-carrying fluids and the energy of eruption of Velican geyser, *J. Volcanol. Geotherm. Res.*, *8*, 267–283.

Stenning, A. (1964), Instabilities in the flow of a boiling liquid, *J. Basic Eng. Trans. ASME Ser. D*, *86*, 213–228.

Thiery, L., and R. Mercury (2009), Explosive properties of water in volcanic and hydrothermal systems, *J. Geophys. Res.*, *114*, B05205, doi:10.1029/2008JB005742.

Vandemeulebrouck, J., P. Roux, and E. Cros (2013), The plumbing of Old Faithful Geyser revealed by hydrothermal tremor, *Geophys. Res. Lett.*, *40*, 1989–1993, doi:10.1002/grl.50422.

Voight, B., et al. (1999), Magma flow instability and cyclic activity at Soufriere Hills volcano, Montserrat, British West Indies, *Science*, *283*, 1138–1142.

Weir, G., R. Young, and P. McGavin (1992), A simple model for Geyser Flat, Whakarewarewa, *Geothermics*, *21*(1-2), 281–304.

White, D. (1967), Some principles of geyser activity, mainly from Steamboat Springs, Nevada, *Am. J. Sci.*, *265*, 641–684.

Woods, A., and S. Bower (1995), The decompression of volcanic jets in a crater during explosive volcanic eruptions, *Earth Planet. Sci. Lett.*, *131*, 189–205.